



MODELING BRIDGMAN HEATING IN THERMOELECTRIC GENERATORS

Edward M. Ledesma,¹ Shervin Sammak,² Matthew M. Barry^{1,*}

¹Department of Mechanical Engineering and Materials Science,
University of Pittsburgh, Pittsburgh, PA 15261, USA

²Center for Research Computing,
University of Pittsburgh, Pittsburgh, PA 15213, USA

ABSTRACT

Thermoelectric generators (TEGs) are small-scale, solid-state devices that convert heat flux into electrical energy through the Seebeck effect. To reliably predict the behavior of these devices under a large range of operational conditions, numeric modeling is often pursued. Within most numerical models, a heat source term is often neglected due to the difficulty of spatially resolving the current density vector. This term represents the Bridgman effect, which is volumetric source term resulting from the gradient of current density vector in the thermoelectric material caused as the system simultaneously tries to maintain both a steady thermal gradient and charge distribution. To investigate the effect of Bridgman heating on the predictions of numeric models of TEGs, a fully coupled thermoelectric model was constructed in ANSYS CFX using the built-in Electromagnetic Model. This model was then used to predict the thermal and electrical performance of single and multi-junction TEGs. Heat generation terms within the energy equation included volumetric expressions for Joule, Thomson and Bridgman heating, and a flux expression for Peltier heating, as well as temperature-dependent thermophysical material properties. The role of Bridgman effect on thermoelectric performance predictions is studied by considering and neglecting the Bridgman effect in the computational analysis. In regions where large current density gradients existed, namely at interfaces between the interconnectors and thermoelectric materials, there is localized Bridgman heating. By considering Bridgman heating, global energy imbalances decreased in all scenarios, upward of 47%, and was more perceptible when the device operates at larger temperature gradients and higher current density values.

KEY WORDS: thermoelectric coupled modeling, thermoelectric generators, finite volume modeling

INTRODUCTION

Thermoelectric generators (TEGs) are solid-state devices that convert heat into electrical power. Through the Seebeck effect, TEGs can power systems in harsh conditions where sunlight does not reach, such as deep-space [1]. Considering the expenses in recreating such conditions for testing purposes and the high cost of thermoelectric materials, it is important to have the capability to accurately model the performance of TEGs over a large range and extreme operational conditions. In 1954, Domenicali laid out the fundamental equations for modeling each of the thermoelectric terms [2]. However, Domenicali's work did not offer a way to combine the Seebeck effect, Joule, Peltier, Thomson and Bridgman heating into a single analytic expression able to predict the thermal and electrical performance of TEG systems. To remedy this, Sutton [3] and Angrist [4] proposed a figure of merit approach for analytic modeling. The figure of merit approach combined Thomson

*Corresponding Matthew M. Barry: matthew.michael.barry@pitt.edu

and Peltier terms into one expression and neglected the Bridgman term. This method proved effective and is still widely used as a simple and quick evaluation of system performance when high accuracy is not necessary. A number of years later, in an effort to improve the accuracy of analytic modeling, Fraisse et al.[5] published a conservation of energy (CoE) approach to TEG modeling. The main difference from the figure of merit approach is that the CoE model had separate terms for Peltier and Thomson heating. Furthermore, in recent years, there has been a growing need for numeric modeling to be able to capture the three-dimensional physics of the system. The earlier papers have asserted that for low temperature TEG devices, Thomson heating can be neglected in their models [6–8]. However, looking at works that specifically study the effect of including the Thomson effect has on numeric modeling, the Thomson effect plays a significant role even at low temperatures, though it is a lesser role when compared to high temperature systems [9]. Furthermore, the same study shows that with increasing temperature difference across the system, the greater impact the Thomson effect has on the model for all calculated parameters. These studies determined under which conditions Thomson heating has a profound effect on the accuracy of the model, primarily being large drops in temperature across the system. To build upon this notion, recent multi-physics numerical modeling [10] in OpenFOAM has been compared against experimental data sets and shown reasonable agreement when considering the Thomson effect. It can be seen that the often-neglected Thomson effect has a substantial role on predictions of device performance. Inasmuch, very less emphasis is given to study and explore the role and need for modeling Bridgman heating on overall performance. Thus, this paper investigates the conditions, if any, in which Bridgman heating would have a significant impact on the model's accuracy and energy imbalances.

METHODOLOGY

2.1 Model

The three-dimensional finite volume method (FVM) model used was built in ANSYS CFX using the Electromagnetic Model (EM). Within the EM model, the electric current density and electric potential are solved for when Maxwell's equations are directly coupled to the thermal energy equation. The CFX model used uniform, orthogonal and conformal hexahedral meshes that were constructed in ANSYS ICEM. All mesh elements had a quality of 0.999951 to 1, with an aspect ratio of 0.999951 to 1, and a skew of unity. Three meshes were used for a grid independence and numerical uncertainty study, all based upon a simple TEG configuration where the n - and p -type legs have a square cross-section measuring 5 mm by 5 mm and are 10 mm in length, and the copper interconnectors were 15 mm by 5 mm by 1 mm. A coarse mesh with geometrical dimensions is shown in Fig. 1 a). The geometries used were a single, two, three, four, and five junction models.

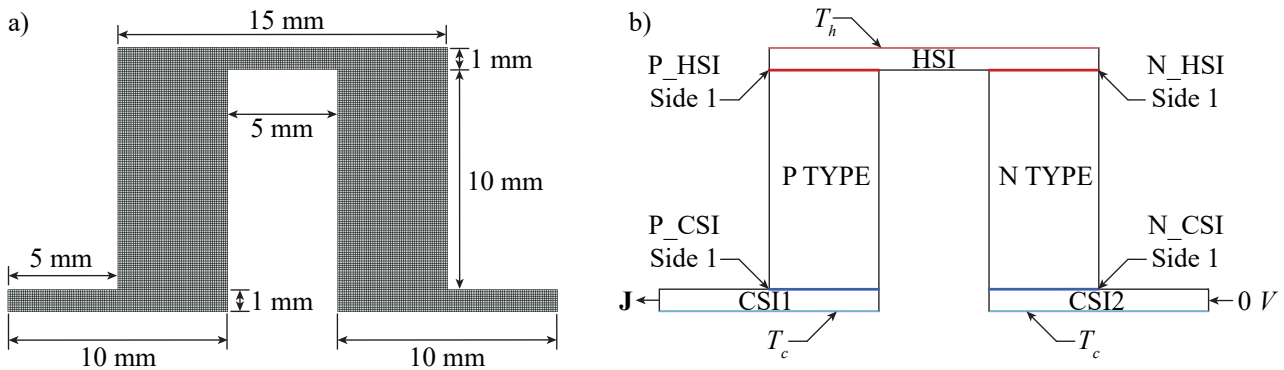


Fig. 1 Representation of a) coarse mesh with geometrical dimensions, and b) domain and surface identifiers used with the numerical model.

2.2 Modeling

ANSYS CFX is a fully-implicit FVM solver that allows for the coupling of the thermal energy and Maxwell's equations via surface and volumetric source terms. The EM model inherently treats Joule heating. Temperature-dependent thermophysical properties were used for the *n*- and *p*-type thermoelectric materials, as well as for the interconnectors, and the polynomial fits of said properties are provided in Tab. 1.

Table 1 Polynomial expressions for temperature dependent thermoelectric properties.

<i>n</i> -type AgPb ₁₈ SbTe ₂₀ [11]		<i>p</i> -type Na _{0.8} Pb ₂₀ Sb _{0.8} Te ₂₂ [12]	
α^n	$= (-3.202118465009907e-19)T^6 + (9.203585371307136e-16)T^5 + (-1.073152310161369e-12)T^4 + (6.493910899794523e-10)T^3 + (-2.15109875689092e-07)T^2 + (3.646981516744837e-05)T + (-0.002561458547361978)$	α^p	$= (-1.500813826446285e-19)T^6 + (4.293338680148655e-16)T^5 + (-5.014714714245148e-13)T^4 + (3.042590912073281e-10)T^3 + (-1.010501330398025e-07)T^2 + (1.822883155906853e-05)T + (-0.001365897370156843)$
λ^n	$= (3.634218867237926e-15)T^6 + (-1.119227631273517e-11)T^5 + (1.410461035072385e-08)T^4 + (-9.307231318913803e-06)T^3 + (0.003396895991439032)T^2 + (-0.6552982139209359)T + (54.70633936832369)$	λ^p	$= (5.238086549608868e-17)T^6 + (-2.927636770231909e-13)T^5 + (5.844390241944433e-10)T^4 + (-5.642804450717544e-07)T^3 + (0.0002909446395983974)T^2 + (-0.08063418038142083)T + (11.00293123390308)$
σ^n	$= (-3.253703447464733e-08)T^5 + (8.721294302777075e-05)T^4 + (-0.09344706416614766)T^3 + (50.97626108178136)T^2 + (-14667.25239632805)T + (1892814.656277739)$	σ^p	$= (1.319288092705862e-10)T^6 + (-3.85669843140294e-07)T^5 + (0.0004638862454473422)T^4 + (-0.297110247163325)T^3 + (109.4552349385509)T^2 + (-22997.10238999909)T + (2309068.907784006)$
Copper			
λ^{int}	$= (1.5625e-5)T^2 - (8.5625e-2)T + 4.0555e+2$		
ρ^{int}	$= (6.7872e-11)T - 3.0865e-9$		

To further incorporate the remaining thermoelectric phenomena, Common Expression Language (CEL) expressions are used to populate the remaining surface and volumetric source terms of the thermoelectric general energy equation, which for steady-state operation is expressed as [2, 13]

$$\nabla \cdot (\lambda A \nabla T) + \rho A \mathbf{J}^2 - T A \mathbf{J} \left[(\nabla \alpha)_T + \left(\frac{\partial \alpha}{\partial T} \right) \nabla T \right] - \alpha T \nabla \mathbf{J} = 0 \quad (1)$$

where the first term represents conduction, the second term Joule heat, the third term Peltier heat, the fourth term Thomson heat, and the fifth term Bridgman heat. Tab. 2 provides the CEL expressions used in each of the unique domains, which are shown in Fig. 1 b), which will be elaborated upon in the following.

To start, the Seebeck voltage, denoted as \mathbf{V}_α , was calculated for each thermoelectric material such that

$$\mathbf{V}_\alpha^{n,p} = |\alpha^{n,p}| \nabla T \quad (2)$$

Table 2 CEL expressions of thermoelectric phenomena. Variables, which are used to evaluate expressions, are italicized. Expression are in *Courier* font, and the “matprop” designation corresponds to the material property polynomial fit defined in Tab. 1. Built-in CEL expressions, two-dimensional and three-dimensional mesh locators are in bold typeset.

Term	CEL Expression
V_{α}^n V_{α}^p	abs(alphaNmatprop*(<i>T.Gradient X</i> + <i>T.Gradient Y</i> + <i>T.Gradient Z</i>) alphaPmatprop*(<i>T.Gradient X</i> + <i>T.Gradient Y</i> + <i>T.Gradient Z</i>)
$SEMF^n$ $SEMF^p$	VSeebeckN*(volume()@N TYPE/area()@N_CSI Side 1) VSeebeckP*(volume()@N TYPE/area()@P_CSI Side 1)
V_{oc}	(volumeInt(SEMFN)@N TYPE/volume()@N TYPE) + (volumeInt(SEMFP)@P TYPE/volume()@P TYPE)
R_{el}^n	(volumeInt(ElectricalResistivityN)@N TYPE/volume()@N TYPE)*((0.01 [m])/(0.005*0.005 [m^2]))
R_{el}^p	(volumeInt(ElectricalResistivityP)@P TYPE/volume()@P TYPE)*((0.01 [m])/(0.005*0.005 [m^2]))
R_{el}^{CSI1}	(volumeInt(ElectricalResistivityInt)@CSI1/volume()@CSI1)*((0.01 [m])/(0.001*0.005 [m^2]))
R_{el}^{CSI2}	(volumeInt(ElectricalResistivityInt)@CSI2/volume()@CSI2)*((0.01 [m])/(0.001*0.005 [m^2]))
R_{el}^{HSI}	(volumeInt(ElectricalResistivityInt)@HSI/volume()@HSI)*((0.015 [m])/(0.001*0.005 [m^2]))
Q_{Thom}^n Q_{Thom}^p	tauNmatprop (<i>T.Gradient X*Current Density X</i> + <i>T.Gradient Y*Current Density Y</i> + <i>T.Gradient Z*Current Density Z</i>) tauPmatprop*(<i>T.Gradient X*Current Density X</i> + <i>T.Gradient Y*Current Density Y</i> + <i>T.Gradient Z*Current Density Z</i>)
Q_{Pelt}^n Q_{Pelt}^p	alphaNmatprop*(<i>T</i>)*(<i>Current Density X</i> + <i>Current Density Y</i> + <i>Current Density Z</i>) alphaPmatprop*(<i>T</i>)*(<i>Current Density X</i> + <i>Current Density Y</i> + <i>Current Density Z</i>)
Q_{Brid}^n Q_{Brid}^p	(<i>T</i>)*alphaNmatprop*(<i>Current Density.Gradient X</i> + <i>Current Density.Gradient Y</i> + <i>Current Density.Gradient Z</i>) (<i>T</i>)*alphaPmatprop*(<i>Current Density.Gradient X</i> + <i>Current Density.Gradient Y</i> + <i>Current Density.Gradient Z</i>)

where $\alpha^{n,p}$ is the Seebeck coefficient for the n - and p -type materials, respectively. The interconnectors were assumed to have negligible Seebeck coefficients, and thus do not contribute to the generation of an electric potential. With a Seebeck voltage distribution prescribed within each thermoelectric material leg, the Seebeck Electromotive Force (SEMF) was calculated as

$$\mathbf{SEMF}^{n,p} = \mathbf{V}_{\alpha}^{n,p} \left(\frac{\nabla^{n,p}}{A^{n,p}} \right) \quad (3)$$

where $\nabla^{n,p}$ is the volume of the n - and p -type legs, respectively, and $A^{n,p}$ is the cross-sectional area of the n - and p -type legs, respectively. Thus, the total Seebeck voltage, often referred to as the open-circuit voltage (which occurs when no load is present) is expressed as

$$V_{oc} = \frac{\int_{\nabla} \mathbf{SEMF}^{n,p}}{\nabla}. \quad (4)$$

The total electrical resistance of each solid domain was set to be the volume integral of the electrical resistance

divided by the square of the cross-sectional area such that:

$$R_{el}^{n,p,CSI1,CSI2,HSI} = \frac{\int_V \rho^{n,p,int}}{(A^{n,p,CSI1,CSI2,HSI})^2}. \quad (5)$$

With the definition of Eqns. 4 and 5, the magnitude of the current density vector \mathbf{J} , which is a scalar value I , is found as:

$$I = \frac{V_{oc}}{(R_{el}^n + R_{el}^p + R_{el}^{CSI1} + R_{el}^{CSI2} + R_{el}^{HSI}) + R_{load}} = \frac{V_{oc}}{R_{in} + R_{load}} \quad (6)$$

where R_{load} is the electrical resistance of the load and R_{in} is the device internal resistance, which is the sum of the electrical resistances of the n - and p -type materials and interconnectors. For maximum power generation, the load resistance was set equal to the internal resistance. The scalar value of current is converted to a current density vector by dividing by the area of the outlet terminal, and by assuming the vector acts normal to the outlet terminal surface as shown in Fig. 1 b). Thus, the current density is defined as:

$$\mathbf{J} = \frac{I}{A_{out}} \quad (7)$$

which when coupled with a zero-voltage potential at the inlet terminal as shown in Fig. 1 b), provides the necessary boundary conditions for Maxwell's equations. It is noted that \mathbf{J} evolves with the solution, and provides the coupling between the thermal and electrical constitutive equations. Furthermore, with the definition of \mathbf{J} , the electric potential \mathbf{E} is able to develop within the system. To provide the thermal boundary conditions, the top of the hot-side interconnector (HSI) is exposed to a constant temperature T_h , and the bottom side of the cold-side interconnectors (CSI), CSI1 and CSI2, are exposed to a constant temperature T_c . All other exterior surfaces are kept adiabatic. Additionally, a conservative interface flux was applied to the thermal and electrical equations at the thermoelectric and interconnector interfaces.

With the aforementioned equations defined, specifically Eqn. 7, the remainder of the surface and volumetric source terms are able to be defined, as well as the system response quantities (SRQs). To define the Thomson heat, the Thomson coefficient must first be defined as

$$\tau^{n,p} = \left(\frac{\partial \alpha^{n,p}}{\partial T} \right) T \quad (8)$$

Thus, the Thomson heat is defined as:

$$Q_{Thom}^{n,p} = -\tau^{n,p} \mathbf{J} \nabla T \quad (9)$$

It is noted that the Thomson heat only occurs in the thermoelectric materials, for those materials have non-zero Seebeck coefficients. Now, the Peltier heat is able to be defined at the interfaces of the thermoelectric materials and interconnectors. The Peltier heat was incorporated into the model as a surface source term. The Peltier heat at the cold-side of the thermoelectric materials acts as a source, while at the hot-side of thermoelectric materials it acts as a sink. The Peltier heat is defined as:

$$Q_{Pelt}^{n,p} = \alpha^{n,p} T \mathbf{J}. \quad (10)$$

The last remaining thermoelectric phenomena, the Bridgman heat, is then defined as:

$$Q_{\text{Brid}} = \alpha^{n,p} T \nabla \mathbf{J}. \quad (11)$$

With all thermoelectric phenomena accounted for, the power output of the device is calculated via the following:

$$P_o = I^2 R_{\text{load}} = \mathbf{J} \cdot \mathbf{E} = Q_h - Q_c. \quad (12)$$

Within Eqn. 12, the three expressions for power - that calculated by the maximum power transfer theorem, that by the dot product of the current density vector and electric field vector, and that by the difference of the heat into HSI and out of the CSIs - could be evaluated. With the definition of the SRQ P_o , the total energy imbalance of the system is then defined as:

$$E_{\text{im}} = \frac{|Q_h - Q_c - P_o|}{Q_h} \quad (13)$$

Within Eqn. 13, the last term of Eqn. 12, i.e. the difference of heat input and output, is used to populate the power output variable. To study the effects of operating temperatures and number of junctions on energy imbalances while considering and neglecting Bridgman heat, T_c was held invariant at 300 K, while T_h was varied between 350 and 700 K. The load resistance was set equal to the internal resistance, as to maximize power output. The convergence criteria for thermal energy and electrical current were set to a maximum value of 1e-10 for the energy equation, electric potential and current density.

RESULTS AND DISCUSSION

The following sections detail the numeric validation and numeric uncertainty quantification of the proposed mode, as well as the effect of thermal boundary conditions and number of junctions on global energy imbalances.

3.1 Validation

The primary reason for conducting the proposed study in ANSYS CFX instead of ANSYS Thermal-Electric (TE), the community accepted FVM solver, is CFX's ability to solve the current density vector and the subsequent incorporation of user-defined heat source terms, thus allowing for the resolution of the Bridgman heat. To ensure that the proposed model accurately predicts thermal-electric performance, the single junction geometry was run without Bridgman heating and compared to results obtained via the use of ANSYS TE, considering the same geometry, boundary conditions and mesh (the coarse mesh, which will be elaborated upon in the following). The results of this comparison, while also considering the analytic solution as presented by Angrist [4], are shown in Fig. 2, where electrical power output, as determined by the second term in Eqn. 12, is shown. It is evident the results from CFX and Thermal-Electric are in good agreement, with CFX being in closer agreement to the analytic solution, supporting the validity of the CFX model. Furthermore, it is evident there is an under-prediction in power output when considering the Bridgman effect in comparison to numerical solvers that do not include the Bridgman heating term, albeit this value is small, on the order of a couple of tenths of a percent decrease at the maximum hot-side temperature.

In addition to validating the proposed model to an already accepted modeling tool, a grid independence and uncertainty quantification study was pursued. In accordance with American Society of Mechanical Engineers standards, a grid convergence index (GCI) value was calculated for each SRQ, and the numeric uncertainty associated with the discretization of the governing partial differential equations into an FVM formulation is

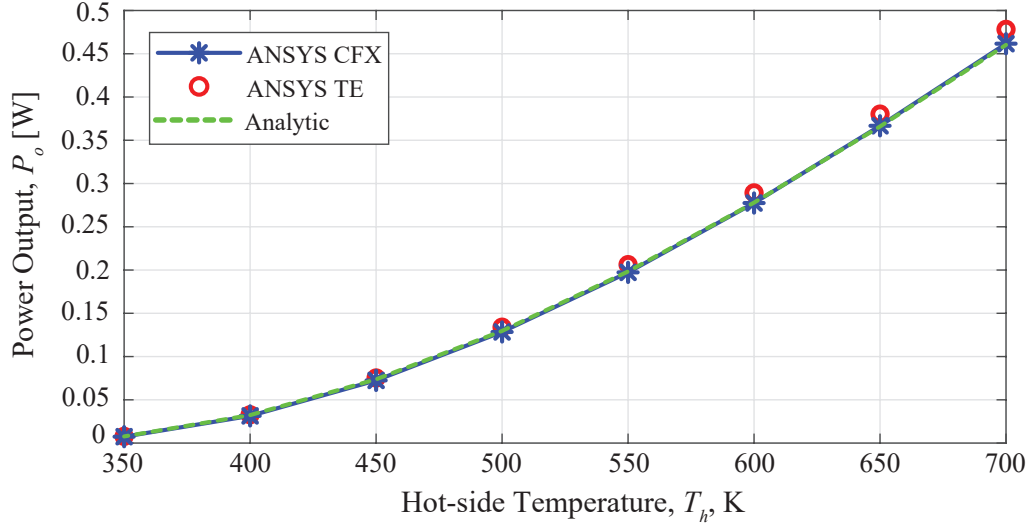


Fig. 2 Comparison of power output predictions obtained by ANSYS Thermal-Electric (TE), ANSYS CFX and analytic, with ANSYS CFX excluding Bridgman heating for a comparable comparison.

provided [14–16]. To quantify the discretization uncertainty, three consecutively refined meshes were used: a coarse mesh with 670,000 elements, a medium mesh with 5,400,000 elements and a fine mesh with 43,200,000 million elements. The findings of these two studies is presented in Tab. 3. It is seen that a grid-independent solution is obtained, and furthermore the uncertainty associated with the numeric results are minimal.

Table 3 Grid independence results and associated numeric uncertainties for all pertinent SRQs. Percent difference reported from un-rounded values. SRQs for AgNa are reported at 700 K.

Property		Analytic	Coarse	Medium	% Diff.	Fine	% Diff.	U_{num} [%]
Thermal	Q_h [W]	3.903	4.121	4.140	0.5	4.147	0.2	0.1
	Q_c [W]	3.443	3.668	3.684	0.4	3.694	0.3	0.6
	Q_{Thom} (W)	1.064	1.053	1.060	0.7	1.064	0.3	0.3
	Q_{Pelt} (W)	-2.008	-1.970	-1.994	1.2	-2.005	0.5	0.6
	Q_{Joul} (W)	0.472	0.462	0.468	1.2	0.470	0.6	0.6
Electrical	\mathbf{E} (V)	-	0.095	0.095	0.9	0.096	0.5	0.6
	V_{oc} (V)	0.193	0.190	0.191	0.9	0.192	0.5	0.6
	\mathbf{J} (A m^{-2})	-	9.781e5	9.807e5	0.3	9.817e5	0.1	0.1
	I [A]	4.892	4.890	4.903	0.3	4.908	0.1	0.1
	R_{int} (Ω)	0.020	0.019	0.020	0.6	0.020	0.4	0.6
Calculated	$P_o = I^2 R_{\text{load}}$ (W)	0.460	0.464	0.469	1.2	0.471	0.6	0.6
	$P_o = \mathbf{J} \cdot \mathbf{E}$ (W)	-	0.462	0.468	1.2	0.470	0.6	0.6
	$P_o = Q_h - Q_c$ (W)	0.460	0.449	0.465	3.5	0.469	0.8	0.3
	$\eta = (I^2 R_{\text{load}})/Q_h$ (%)	11.792	11.248	11.325	0.7	11.368	0.4	0.6
	$\eta = (\mathbf{J} \cdot \mathbf{E})/Q_h$ (%)	-	11.221	11.299	0.7	11.343	0.4	0.6
	$\eta = (Q_h - Q_c)/Q_h$ (%)	11.792	10.896	11.231	3.0	11.306	0.7	0.2

3.2 Global Energy Imbalances

To ascertain the effect of hot-side temperature on a single junction device, T_h was varied between the previously established range, and the global energy imbalance defined by Eqn. 13 was determined. The trend of global energy imbalance versus T_h for situations considering and neglecting Bridgman heating is shown in Fig. 3 a). Given the magnitude of the energy imbalance, it is seen that the inclusion of the Bridgman effect

significantly impacts the model's ability to balance energy for all geometries at higher temperatures, much like Thomson heating. Taking the maximum case of $T_h=700$ K, the inclusion of the Bridgman heating terms reduces the global energy imbalance by 47%. Conversely, taking the minimum case of $T_h=350$ K, considering the Bridgman heat terms increase the energy imbalance by 275%. When considering the Bridgman effect on the global energy imbalances over the range of hot-side temperatures, said imbalances appear rather invariant and average below 0.20%. Conversely, when the Bridgman effect is not considered, the global energy imbalances appreciably increase with increasing hot-side temperatures. Thus, it is evident that in the study of generators operating at large temperature gradients, the inclusion of the Bridgman effect will aid in the reduction of global energy imbalances.

Similarly, when considering the global energy imbalance as a function of number of junctions, an increase in junction counts results in a decrease of global energy imbalances. This is shown in Fig. 3 b). After two junctions are considered, the global energy imbalances approach a constant value, due to the periodic nature of the TEG structure. These results are as expected, for the Bridgman effect is a function of temperature and current density. With increasing junction count, the temperature difference across the device remains unchanged, and the current density remains constant.

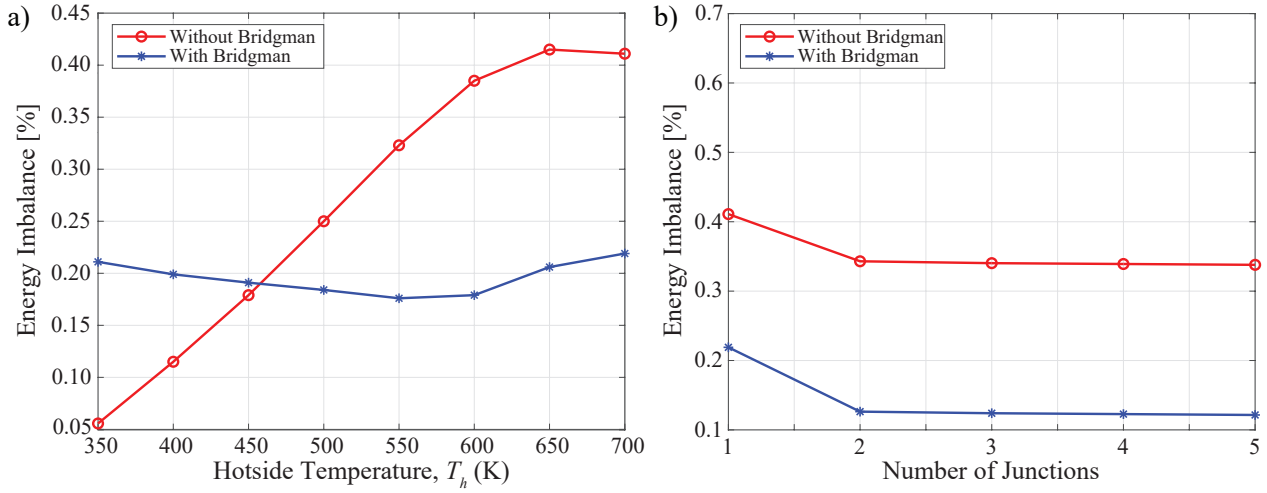


Fig. 3 Comparison of global energy imbalance considering and neglecting Bridgman heating for for a) varying hot-side temperatures, and b) varying number of junctions.

The marked decrease in the global energy imbalance is due to the inclusion of all thermoelectric phenomena when evaluating device performance. As outlined by Domenicali [2], all thermoelectric phenomena – Joule, Peltier, Thomson and Bridgman effects – are present during device operation, as described by Eqn. 1. For the thermoelectric conservation of energy equation to be satisfied, and for the power output to be identically equal to the difference of heat input and output, all pertinent effects must be modeled.

CONCLUSIONS

To study the effect of the inclusion of Bridgman heating on TEG performance, a fully-coupled thermal-electric finite volume method model was developed in ANSYS CFX. The proposed ANSYS CFX model utilized the Electromagnetic Model, which allowed for the resolution of the three dimensional current density vector, and subsequently the Bridgman heating term. To fully evaluate the effect of Bridgman heating on TEG performance and model energy imbalances, devices comprised of one through five junctions, in one junction increments, were studied under various hot-side temperatures. It was found that the inclusion of the Bridgman effect in the finite volume model reduced the the power output of the device. Additionally, the omission of the Bridgman effect led to higher global energy imbalances within the numeric model, which was more pronounced at higher device hot-side temperatures. Considering the Bridgman effect reduced global energy

imbalances by 47% at the maximal hot-side temperature. Lastly, upon modeling multiple junctions within the TEG, the model global energy imbalances decrease to a constant, minimum value. For high-fidelity numeric models of TEGs operating at high temperatures, modeling of the Bridgman effect is necessary for minimizing model energy imbalances and increasing confidence in predictions.

ACKNOWLEDGMENTS

Funding for the current work was provided by the Mascaro Center for Sustainable Innovation (MCSI) at the University of Pittsburgh. Computational resources and support were provided by the Center for Research Computing (CRC) at the University of Pittsburgh.

NOMENCLATURE

Variables

A	cross-sectional area	(m ²)	R	electrical resistance	(Ω)
E	electrical potential	(V)	SEMF	Seebeck electromotive force	(V)
E_{im}	energy imbalance	(-)	T	temperature	(K)
I	electrical current	(A)	U_{num}	numeric uncertainty	(%)
\mathbf{J}	current density vector	(Am ⁻²)	\forall	volume	(m ³)
P_o	power output	(W)	V_α	Seebeck voltage	(V)
Q	heat	(W)	V_{oc}	open-circuit voltage	(V)

Subscripts and Superscripts

Brid	Bridgman	load	load
c	cold-side	n	n -type
el	electrical	out	outlet terminal
h	hot-side	p	p -type
in	internal	Pelt	Peltier
int	interconnector	Thom	Thomson
Joul	Joule		

Greek Letters

α	Seebeck coefficient	(VK ⁻¹)	ρ	electrical resistivity	(Ω m)
η	thermal conversion efficiency	(-)	σ	electrical conductivity	(Sm ⁻¹)
λ	thermal conductivity	(Wm ⁻¹ K ⁻¹)	τ	Thomson coefficient	(VK ⁻¹)

Acronyms

CEL	Common Expression Language	GCI	grid convergence index
CSI	cold-side interconnector	HSI	hot-side interconnector
EM	Electromagnetic Model	SRQ	system response quantity
FVM	finite volume method	TE	Thermal-Electric

REFERENCES

- [1] G. Bennett, J. Lombardo, R. Hemler, G. Silverman, C. Whitmore, W. Amos, E. Johnson, A. Schock, R. Zocher, T. Keenan, *et al.*, “Mission of daring: the general-purpose heat source radioisotope thermoelectric generator,” in *4th International Energy Conversion Engineering Conference and Exhibit (IECEC)*, p. 4096, 2006.
- [2] C. A. Domenicali, “Irreversible thermodynamics of thermoelectricity,” *Reviews of Modern Physics*, vol. 26, no. 2, p. 237, 1954.
- [3] G. W. Sutton, *Direct energy conversion*. New York, McGraw-Hill Book Company, 1966.
- [4] S. W. Angrist, *Direct energy conversion*. Allyn and Bacon, Inc., Boston, 1976.
- [5] G. Fraisse, J. Ramousse, D. Sgorlon, and C. Goupil, “Comparison of different modeling approaches for thermoelectric elements,” *Energy conversion and management*, vol. 65, pp. 351–356, 2013.
- [6] N. Espinosa, M. Lazard, L. Aixala, and H. Scherrer, “Modeling a thermoelectric generator applied to diesel automotive heat recovery,” *Journal of Electronic materials*, vol. 39, no. 9, pp. 1446–1455, 2010.
- [7] D. Tatarinov, M. Koppers, G. Bastian, and D. Schramm, “Modeling of a thermoelectric generator for thermal energy regeneration in automobiles,” *Journal of electronic materials*, vol. 42, no. 7, pp. 2274–2281, 2013.
- [8] S. Kumar, S. D. Heister, X. Xu, J. R. Salvador, and G. P. Meisner, “Thermoelectric generators for automotive waste heat recovery systems part i: numerical modeling and baseline model analysis,” *Journal of electronic materials*, vol. 42, no. 4, pp. 665–674, 2013.
- [9] M. Zhang, Y. Tian, H. Xie, Z. Wu, and Y. Wang, “Influence of thomson effect on the thermoelectric generator,” *International Journal of Heat and Mass Transfer*, vol. 137, pp. 1183–1190, 2019.
- [10] B. Pfeiffelmann, A. C. Benim, and F. Joos, “A finite volume analysis of thermoelectric generators,” *Heat Transfer Engineering*, pp. 1–9, 2018.
- [11] K. F. Hsu, S. Loo, F. Guo, W. Chen, J. S. Dyck, C. Uher, T. Hogan, E. K. Polychroniadis, and M. G. Kanatzidis, “Cubic agpbmsbte_{2+m} : bulk thermoelectric materials with high figure of merit,” *Science*, vol. 303, no. 5659, pp. 818–821, 2004.
- [12] P. F. Poudeu, J. D’Angelo, A. D. Downey, J. L. Short, T. P. Hogan, and M. G. Kanatzidis, “High thermoelectric figure of merit and nanostructuring in bulk p-type $\text{na}_{1-x}\text{pbmsbytem}_{2+2}$,” *Angewandte Chemie International Edition*, vol. 45, no. 23, pp. 3835–3839, 2006.
- [13] A. Chakraborty, B. Saha, S. Koyama, and K. Ng, “Thermodynamic modelling of a solid state thermoelectric cooling device: Temperature–entropy analysis,” *International Journal of Heat and Mass Transfer*, vol. 49, no. 19, pp. 3547–3554, 2006.
- [14] P. J. Roache, “Perspective: a method for uniform reporting of grid refinement studies,” *Journal of Fluids Engineering*, vol. 116, no. 3, pp. 405–413, 1994.
- [15] C. J. Roy and W. L. Oberkampf, “A comprehensive framework for verification, validation, and uncertainty quantification in scientific computing,” *Computer Methods in Applied Mechanics and Engineering*, vol. 200, no. 25, pp. 2131 – 2144, 2011.
- [16] I. B. Celik, U. Ghia, and P. J. Roache, “Procedure for estimation and reporting of uncertainty due to discretization in cfd applications,” *Journal of fluids Engineering-Transactions of the ASME*, vol. 130, no. 7, p. 078001, 2008.